Supporting Information

Karthigeyan et al. 10.1073/pnas.1402695111

1. SI Results and Discussion

1.1. Comparison of Inhibitory Activity of Felodipine with Commercially Available Inhibitors. Kinase assays were performed (autoradiogram in Fig. S3*A*) in the presence of either DMSO (Sigma) (Fig. S3*A*, lane 3)/felodipine 10 μM and 20 μM (Fig. S3*A*, lanes 4 and 5) or MLN8237 0.1 μM and 1 μM (Fig. S3*A*, lanes 1 and 2). This is in agreement with the published results for MLN8237 (1). Both felodipine and MLN8237 can inhibit Aurora A but cannot affect the kinase activity of Aurora B (autoradiogram in Fig. S3*B*). The Aurora A kinase activity is dependent on the autophosphorylation at Thr-288 in its activation loop (2).

1.2. In Vitro Kinase Assay. Felodipine may also inhibit the autophosphorylation of Aurora A in a dose-dependent manner, in vitro, which is comparable to its substrate (histone H3) phosphorylation inhibition (in the autoradiogram in Fig. S3*C*, compare lane 2 with lanes 3–8). The IC_{50} of felodipine was ∼20 μM in the kinase assay using the inhibition of Aurora A autophosphorylation (Fig. S3*D*). Collectively, these results suggest that felodipine selectively inhibits Aurora A but not B in vitro. Felodipine was tested against a selective panel of kinases, as listed in Table S1 at a concentration of 20 μM. Among the tested kinases, felodipine inhibits only LCK kinase and VEGF-R2 kinase comparable to Aurora A kinase at this concentration, whereas the rest of the kinases are not significantly affected. To test the effects of these small molecules on Aurora A inside the cell, we treated HeLa cells preexposed to nocodazole (mitotic phase synchronization) for 12 h before incubation with felodipine (20 μM) and with 20 μM MG132 for 3 h in the presence of nocodazole before harvesting the cells. Western blot analysis was performed using the anti-pThr-288 Aurora A antibody as a biomarker (degree of autophosphorylation) for Aurora A activity and anti-GAPDH for the loading control (Fig. S4*A*). The results showed significant inhibition of Aurora A autophosphorylation only in the cells treated with felodipine (Fig. S4*A*, lane 2) compared with cells treated with DMSO only (Fig. S4*A*, lane 1).

1.3. Kinase Assay in a Cellular System. To investigate the effect of felodipine in a cellular system, the mitotic phosphorylation was analyzed by a Western blot analysis using anti-MPM2 antibody to compare the DMSO with felodipine/MLN8237-treated HeLa cells (Fig. S4*B*). A similar analysis of a specific substrate of Aurora A other than autophosphorylation was performed. HeLa cells were treated with DMSO or 20 μM felodipine (Fig. S4*C*) and Western blot analysis performed using the anti–ph-TACC3 and α-tubulin antibody as the loading control, which also showed inhibition of phosphorylation [in Fig. S4*C*, compare lanes 2 and 3 in the ph-TACC3 (Ser-558) gel]. In a parallel assay the ph-TACC3 level was scored using the immunostained HeLa cells preexposed to nocodazole based on the fluorescence intensity over the centrosomal body of dividing cells ($n = 100$). As shown in Fig. S4*D*, after treatment with an increasing concentration of felodipine, the number of cells positive for this staining decreased. Moreover, the number of cells with low and medium intensity was relatively higher compared with the number of centrosomes that showed high-intensity fluorescence. Similarly, asynchronous HeLa cells were treated with either 20 μM felodipine for various time points (Fig. S4*E*) or treated for 24 h using the indicated concentrations of felodipine (Fig. S4*F*). Western blot analysis was performed using antibodies recognizing pSer 10 on histone H3 (ph-H3) using the cell lysates. The anti-histone H3 antibody was used as the loading control. In the time-course assay an initial increase in the ph-H3 levels was noticed by 1 h posttreatment. However, a subsequent reduction in the marker was observed up to 24 h posttreatment. Similarly, a dose-dependent reduction in the ph-H3 was observed in the cell lysates treated with 20 and 40 μM felodipine (in Fig. S4*B*, compare lanes 2 and 3 with lane 1 in the α-tubulin gel) compared with cells treated with DMSO (Fig. S4*B*, lane 3). The cellular IC_{50} for Aurora A and B was determined using the ph-T288 and ph-H3S10 mark, respectively (Fig. S4*G*). These data suggest that felodipine also inhibits the Aurora A activity in the cellular system.

1.4. Molecular Docking and Molecular Dynamics Simulation of the Secondary Sites of Binding. Understanding that felodipine binds to the surface pocket surrounded by the residues Phe-157, Ile-158, and Tyr-212, we decided to test the binding within similar surface pockets that exist on human Aurora A. The molecular docking by Autodock (3) showed the majority of the population docked to either the previously mentioned hinge pocket or the pocket over the N-terminal domain surrounded by the residues Trp-128 and His-201. The docked pose is shown in Fig. S7*A*. This pocket also differs from human Aurora B due to the side chain variations between the two kinases (Fig. S7*B*). The molecular dynamics (MD) simulation shows the stability of felodipine in this pocket over a time period of 2 ns (Fig. S7*C*). We also decided to investigate another hydrophobic site, which is formed by the combination of Try-334 and Tyr-338. However, the MD simulation shows that felodipine is not stable over this pocket (Fig. S7*D*).

1.5. Inhibition Kinetics of Felodipine. Because felodipine is not an ATP analog and the findings from our in silico and in vitro studies were suggestive of an uncompetitive mechanism of inhibition, we assessed the kinetic behavior of felodipine-mediated inhibition of Aurora A kinase. Based on the kinetic parameters represented in Fig S8*B*, we concluded that felodipine inhibits Aurora A in a mixed fashion. Further the isothermal calorimetric titration revealed that felodipine has a stochiometry of $n = 2$ binding sites (Fig. S8*C*).

1.6. Felodipine Induces Spindle Pole Defects and Cell Death and Further Retards Tumor Progression. The effects of felodipine on the cell cycle were explored by FACS analysis using five different cell lines: HeLa, HEK293T, MCF7, HCT116, and C6 cells. The results showed that felodipine may induce a dose-dependent increase in aneuploidy compared with DMSO control. In the case of HeLa cells, the 2–4 and >4 N population of cells increased after treatment with felodipine compared with the cells treated with DMSO which had a 2 and 4 N DNA content. In HEK293T cells after treatment with felodipine, the 2N population decreased signicantly, whereas the 2–4, 4, and >4 N population increased with an increasing concentration of felodipine compared with the cells treated with DMSO. Similarly, the 2–4 and >4 N populations in MCF7 and HCT116 both showed a dramatic increase in felodipine-treated cells compared with the DMSO-treated cells (Fig. S9*A*). To further confirm the cell cycle stage in which felodipine treatment shows arrest, we performed a G2/M block using HEK293T cells and then subsequently released the cells after 12 h of treatment with 100 ng/mL nocodazole in the presence of either DMSO or 20 μM felodipine or 100 ng/mL nocodazole (Fig. S9*B*). At the end of the 24 h, the cells were fixed in ethanol and stained with propidium iodide to analyze their DNA content to assign the percentage of cells that reside across the different stages of cell cycles. The results tabulated from the FACS analysis showed that 37% of the cells treated with felodipine remained in the G2/M stage, similar to the nocodazole-treated cells of which nearly 58% cells were arrested in the G2/M stage; whereas only 27% of the whole population was present in the DMSO-treated cells (Fig. S9*C*). These data suggest that felodipine acts at the G2-to-M transition level where Aurora A is expected to exhibit peak activity during the cell cycle.

The spindle pole morphology in HeLa cells, after felodipine treatment by immunocytochemistry analysis, was investigated using the anti–α-tubulin antibody. Confocal microscopic images obtained from the cells treated with 10 μM felodipine were compared with DMSO-treated cells only. Cells with DMSO treatment showed classical bipolar spindle assembly in dividing cells but defects such as monopolar and multipolar spindle were observed in felodipine-treated cells as shown in 40× magnification in Fig. S10*B*. To obtain a better visualiziation, coimmunofluorescence images were captured at 100× magnification using anti–α-tubulin and anti-Aurora A antibodies (Fig. S10 *C* and *D*). The relationship between felodipine treatment and the onset of spindle defects was unambiguously established through the manual quantification of these defects (both monopolar as well as multipolar spindles), using the same images obtained from the previous experiment. Approximately 40% of the dividing cells exhibited defective spindle morphology compared with DMSO-treated cells (Fig. S10*E*). The results obtained from the cellular system encouraged us to investigate the effect of felodipine over the tumor progression rate. Thus, we s.c. administered felodipine on a daily basis to the nude mice that were xenografted with C6 glioma cells. The tumor progression rate and the corresponding immunohistochemical (IHC) analysis of the ph-H3S10 marker in the sections obtained from the corresponding tumor tissue are shown in Fig. S10 *F* and *G*, respectively. The statistical analysis performed with the IHC images (Fig. S10*H*) showed that felodipine can also block the cellular proliferation in vivo.

1.7. Advantages and Limitations of Surface-Enhanced Raman Spectroscopy. Surface-enhanced Raman spectroscopy (SERS) is a form of Raman spectroscopy which is dependent on the high electromagnetic field in the vicinity of the metallic surface with nanoscale roughness to achieve a high Raman cross-section (4). It produces routine enhancements on the order of more than 10^4–10^6 with a maximum enhancement as high as 10^{12} (5). This high enhancement in SERS signals can lead to ultra-low detection of analyte molecules and even down to single-molecule detection (5). The very important point of SERS, especially in the case of therapeutically important proteins, is that it can be performed in a physiological environment and in the active state of the protein. This makes it possible to analyze protein–ligand interactions at significantly lower concentrations compared with NMR and X-ray crystallography. This, combined with the knowledge of the structure of the protein and MD simulation, becomes a potential tool for drug discovery. A thorough understanding of SERS activity in proteins by isotopic substitution to understand the origin of these modes can provide a credible platform for routine use of SERS. Numerous groups have demonstrated that Raman spectroscopy provides information about the secondary and tertiary structure of the protein and the relative abundance of the different amino acids present in protein (6). However, in the case of SERS, it is not always possible to assess all of the vibrational modes of a protein, with the exception of the regions close to the nanoparticle surface (7). The limited information obtained from SERS may be necessary and sufficient to derive important information about the protein without a complete Raman mode analysis. The most prominent modes observed in SERS consist of the amide modes (I, II, and III), which are combination modes of C=O and N–H bonds, are sensitive to hydrogen bonding, and consequently provide information about the secondary structures of proteins. Surface selection rules serve an important role in SERS (8) because different modes of the amino acid residues Phe, Tyr, Trp, and His can be present or absent in the spectrum, depending on their orientation with respect to the nanoparticle surface. This surface-sensitive information can be effectively used for deducing any small molecule binding to the protein which generates two probable scenarios. First, the bound ligand may shift certain resides away from the nanoparticle surface thus obscuring these modes. A few modes of the ligand may be observed in the spectra instead. Second, the bound ligand may completely change the orientation of the protein with respect to the nanoparticle surface. This is due to the fact that the binding of the protein to the nanoparticle is governed by electrostatic as well as hydrophilic/hydrophobic interactions, which might be altered due to ligand binding. The change in spectra thus provides important information on ligand binding and the type of binding on the protein. Preliminary knowledge of the structure of the protein significantly aids in the understanding of the protein interactions at very low concentrations and with high sensitivities in its active state. Because it is a surface-related phenomenon, SERS is very effective for studying surface-binding small molecules. On the contrary, the major limitations of SERS include inability to predict the exact binding of the ligands when the binding site lies deep within the catalytic pocket. Even if the binding of the ligand occurs on the surface, it may not be detected by SERS if this site does not coincide with the binding of the protein to the nanoparticle surface. In this case, specific chemical functionalization of the protein surface is warranted to understand such a binding. Unlike other spectroscopic techniques such as fluorescence, the binding affinity of the ligand cannot be quantitatively predicted.

We have seen that nitrendipine, which has replaced the chlorine atoms of felodipine with a nitro group at the meta position, and is a generic drug for hypertension, shows a reduced affinity compared with felodipine. This is due to the relative ease of rotation of the phenyl ring due to the removal of the steric hindrance caused by having two chlorine atoms at *ortho* and *meta* positions. This suggests that the locking of the phenyl rings at 90° of each other provides the ideal space to dock at said pocket. This is clearly reflected in the SERS spectra of the nitredipine Aurora A composite (part of the thesis of S. Siddhanta) (9). This suggests the possibility of modifying the felodipine or analogous molecule for potential drug applications.

2. SI Materials and Methods

2.1. Purification of Enzymes and Substrates and Kinase Assay. Aurora A and B enzymes expressed as C-terminal His_6-tagged proteins were purified using Ni·nitrilotriacetic acid affinity purification from the respective, recombinant baculovirus-infected Sf21 cells (10). The bacterially expressed recombinant histone (*Xenopus*) H3, which exists in inclusion bodies, was purified by the denaturation in 8 M urea followed by renaturation as described elsewhere (11). H3 was dialyzed against the buffer containing 10 mM Tris·HCl (pH 7.5), 100 mM NaCl, 20% glycerol (vol/vol), 0.05% Nonidet P-40, 0.02% 2-Mercaptoethanol, and 1 mM EDTA; and analyzed using 15% PAGE. Aurora A kinase mutants were created using a site-directed mutagenesis (QuickChange, Agilent) kit in the pET21b-Aurora A-His backbone and expressed in *Escherichia coli*.

2.2. Kinase Assay. One microgram of bacterially expressed recombinant histone H3 was incubated along with either Aurora A (40 ng) or B (40 ng) in a 30-μL reaction mixture containing 50 mM Tris·HCl, 100 mM NaCl, 0.1 mM EGTA, 10 mM $MgCl_2$, 0.2% 2-Mercaptoethanol, and [γ-^{32}P] ATP (specific activity 3.5 Ci/mMol). The reaction mixture and varying concentrations of felodipine were incubated at 30 °C for 5 min followed by the addition of [γ-^{32}P] ATP and an additional incubation of 10 min. The reaction mixture was precipitated using 25% (wt/vol) trichloroacetic acid and resolved using 15% PAGE followed by autoradiography. The intensity of the signal was quantified using a PhosphorImager analyzer (Fuji) and the same data were plotted as a bar chart. IC_{50} was calculated based on the Aurora A autophosphorylation without the substrate histone H3 in a similar assay. For kinetic analysis, increasing concentrations of [γ-^{32}P] ATP (0–120 μM) were used in the presence of either DMSO or 10, 20, and 40 μM inhibitor in the reaction mixture, which contained a constant amount of enzyme and the other substrate histone H3. The reaction was allowed to proceed for 30 min and subjected to autoradiography. Kinetics was analyzed using the Michaelis–Menten plot to determine the inhibition pattern.

2.3. Isothermal Calorimetry. Freshly purified Aurora A was dialyzed extensively against 20 mM Tris·HCl, pH 8.0, 0.2 mM EDTA, and 100 mM KCl before isothermal titration calorimetry (ITC); 4.2 μM protein in the cell was titrated against 100 μM felodipine in a Microcal ITC 200 microcalorimeter at 25 °C with a stirring speed of 300 rpm. Aurora A and felodipine solutions for ITC were diluted in the final dialysate to prevent artifacts from minor differences in buffer composition. The concentration of DMSO was kept the same in the cell and the syringe (0.2%) to rule out any interference that might arise due to a mismatch of the concentration of DMSO. The samples were thoroughly degassed before titration. The dilution of 100 μM felodipine in dialysate containing an equal percentage of DMSO served as the control. The resulting thermogram (background enthalpy subtracted) was analyzed using the one-set-of-binding-sites model of Levenberg–Marquardt nonlinear least-squares curve-fitting algorithm, inbuilt in the MicroCal LLC software.

2.4. Cell Culture, Treatment, Immunoblotting Analysis, and FACS Analysis. All mammalian cells were grown and maintained at 37 °C in a 5% CO_2 incubator using DMEM (Sigma) with 10% FBS (HyClone). For the treatment, 1×10^5 cells were seeded in 30-mm dishes. Twenty-four hours after seeding, either DMSO or an increasing concentration of the compound was added and further incubated for 36 h for FACS analysis. For the Western blot analysis, the treatment was given for three hours in the presence of proteosomal block MG132 after arresting the cells in M phase using 200 ng/mL nocodazole for Western blotting, using the anti–phospho-Thr-288 Aurora A and anti–phospho-TACC3 antibody. For H3 S10, Western blot cells were treated for 24 h at indicated concentrations and probed using anti-H3 S10 phospho antibody. For cell cycle analysis, the cells were trypsinized using 0.25% trypsin (Sigma) to collect the cells, washed with PBS, and fixed overnight in 70% (vol/vol) ethanol at −20 °C. They were subsequently stained with (6 μM/mL) propidium iodide (Sigma) and RNase treatment was simultaneously given using (10 μg/mL) RNase A (Sigma) and analyzed in BD FACSCalibur (BD Biosciences) using Cell Quest software (BD Biosciences).

2.5. 3-(4,5-Dimethylthiazol-2-yl)-5-(3-Carboxymethoxyphenyl)-2-(4-Sulfophenyl)-2H-Tetrazolium (MTS) Assay and Immunofluorescence. ***MTS assay.*** Cells (1×10^3) were seeded in 96-well plates and incubated in DMEM containing 5% (wt/vol) FBS with 5% CO_2 at 37 °C in an incubator. After 24 h the cells were treated with DMSO/felodipine and maintained for 24 h. Subsequently, 20 μL CellTiter 96 AQueous One reagent (Promega) was added to each well and processed per the manufacturer's instructions. Considering the untreated wells as 100% viable, a graph was plotted using the absorbance values obtained from treated wells in terms of percent viability.

Immunofluorescence. Coverslip cultures of HeLa cells were treated with DMSO or 10 μM felodipine for 24 h. After treatment, the cells were fixed in 4% (wt/vol) paraformaldehyde and permeabilized with 0.1% Triton X-100. After blocking with 5% FBS, the cells were incubated with anti–α-tubulin monoclonal antibody (DM1A; Calbiochem) for 1 h. These cells were further incubated with Alexa Fluor (488 nm)-conjugated anti-mouse antibody (Invitrogen) for 1 h and stained with Hoechst (Sigma) for 20 min and mounted on slides. Confocal microscopic images were captured (Zeiss LSM Meta 510) and manually scored for spindle pole defects. The numbers of cells showing spindle defects were counted across different fields, for which a histogram of percent abnormal mitotic cells over the total number of mitotic cells was plotted. The statistically significant difference between the control and the treated cell populations was obtained using P values calculated from a t test performed over four independent biological replicates and a sample size of 50 mitotic cells treated with either DMSO or felodipine-treated cells.

2.6. Animal Experiment. Six-week-old NIH strain nude mice were procured from the National Institute of Virology and injected with 10^6 Rat C6 glioma cells. The final concentration was adjusted to 10^6 cells per 200 μL. An equal volume of ECM gel from Engelbreth-Holm-Swarm mouse sarcoma was added and injected into the left flank of mouse s.c. tissue. After 1 wk, DMSO was administered to three mice and felodipine administered to three other mice (5 mg/kg body weight) daily for a 4-wk period. The tumor volume was measured at weekly intervals and plotted as the rate of tumor progression in percentage versus the number of days posttreatment in weeks. All experiments were performed per committee for the purpose of control and supervision of experiments on animals guidelines.

2.7. Raman and SERS. Silver solution was prepared using the method of Lee and Meisel (12). SERS spectra were recorded in a custom-built Raman system (13) using 180° backscattering geometry and a 632.8-nm He–Ne laser (Research Electro Optics, Inc.) as the Raman excitation source. A 60× infinity-corrected objective (Nikon Plan Apo; N.A. 0.9) with 5-mW laser power at the sample was used. The samples were prepared by concentrating the silver nanoparticles and maintaining the concentrated nanoparticle solution to an analyte ratio of 4:1 (vol/vol). These spectra were obtained with 40 ng/μL Aurora A/B with or without 1 μM felodipine/reversine. The typical accumulation time was 30s.

2.8. MD Simulations. The human Aurora A crystallographic structure [Protein Data Bank (PDB) ID code 1MQ4] (14) was used for the initial coordinates of the MD simulations. The electronic structure-optimized (B3LYP/6–31G*) ligand and the protein form the model complex in our simulation, whereas the respective interactions were duly approximated by CHARMM22 force-field parameters (15), including cross-term energy correction map correction (16). Before performing MD of ligand-bonded protein, the ligand-free crystallographic protein structure was neutralized with counterions and solvated with 32016 TIP3P (17) water molecules. Particle Mesh Ewald was used to calculate long-range electrostatic interactions (18). The SHAKE method was applied for fixing the bond lengths involving a hydrogen atom (19). A box cutoff length of 20 Å was adapted during the simulation. After 500,000 steps of energy-minimization, a 1-ns equilibration MD run was performed with a 1 fs unit step size at 300 K. Subsequently the obtained structure was used for molecular docking studies.

The optimized structure of ligand was docked into the protein using the Autodock (Version 4.2) (20). AutoDockTools 1.5.4 (21) was used to set the rotatable bonds and add polar hydrogen. Gasteiger charge was added and the protein was embedded in a grid box with dimensions 126 × 126 × 126, which was centered on the mass center of the protein with a grid spacing of 0.375 Å. The Lamarckian genetic algorithm (22) was used to generate the ligand–protein conformation. Docking was performed with a population size of 300 with 25×10^5 evaluations and a maximum of 27,000 generations. Cluster analysis was performed with an rmsd tolerance of 2 Å. The best conformation is considered to be the conformation with the lowest free binding energy or the lowest energy conformation of the most populated cluster. Finer docking was achieved by maintaining the center of the smaller grid box with dimensions 60 × 60 × 60 at the ligand position of the lowest binding energy.

The resulting coordinates of the docked complex were secured for additioinal MD runs. The entire complex was energy-minimized, followed by a 2-ns MD run at 300 K to capture the required dynamics for our simulation studies. All essential MD procedures were performed with the NAMD program suite (Version 2.8) (23). Corresponding topology and parameter files for MD were generated with the paratool plugin in the VMD visualization program (24), whereas the missing hydrogens of the crystal structure were incorporated using the psfgen plugin. The ab initio electronic structure of the ligand was obtained using Gaussian 09 (25).

2.9. IHC and Histopathological Analysis. Tissues collected in 5% (vol/vol) buffered formalin solution were dehydrated, paraffin embedded, and sectioned using Leica microtome. Five-micron sections of tissue were fixed on glass slides at 55 °C and deparaffinized. Subsequently IHC analysis was performed with an LSAB+System+HRP kit (Dako) exactly per the manufacturer's protocol using the indicated antibodies. The staining pattern was visualized and manually quantitated. A statistical analysis was performed with three independent tumor sections at 40× magnification and the ratio of the total number of 3,3′-diaminobenzidine (+) nuclei versus total number of nuclei was calculated and expressed as the percent nuclear positive.

1. Manfredi MG, et al. (2011) Characterization of Alisertib (MLN8237), an investigational small-molecule inhibitor of aurora A kinase using novel in vivo pharmacodynamic assays. *Clinical Cancer Research* 17(24):7614–7624.
2. Ohashi S, et al. (2006) Phospho-regulation of human protein kinase Aurora-A: Analysis using anti-phospho-Thr288 monoclonal antibodies. *Oncogene* 25(59):7691–7702.
3. Morris GM, et al. (2009) AutoDock4 and AutoDockTools4: Automated docking with selective receptor flexibility. *J Comput Chem* 30(16):2785–2791.
4. McCall SL, Platzman PM, Wolff PA (1980) Surface enhanced Raman scattering. *Phys Lett A* 77(5):381–383.
5. Nie S, Emory SR (1997) Probing single molecules and single nanoparticles by surface-enhanced Raman scattering. *Science* 275(5303):1102–1106.
6. Barth A, Zscherp C (2002) What vibrations tell us about proteins. *Q Rev Biophys* 35(4):369–430.
7. Schatz G, Young M, Duyne R (2006) Electromagnetic mechanism of SERS. *Surface-Enhanced Raman Scattering,* Topics in Applied Physics, eds Kneipp K, Moskovits M, Kneipp H (Springer, Berlin), Vol 103, pp 19–45.
8. Suh JS, Moskovits M (1986) Surface-enhanced Raman spectroscopy of amino acids and nucleotide bases adsorbed on silver. *J Am Chem Soc* 108(16):4711–4718.
9. Siddhanta S (2014) Application of Raman and surface enhanced Raman spectroscopy in probing biomolecular interactions. PhD thesis (Jawaharlal Nehru Centre for Advanced Scientific Research, Bangalore, India).
10. Kishore AH, et al. (2008) Specific small-molecule activator of Aurora kinase A induces autophosphorylation in a cell-free system. *J Med Chem* 51(4):792–797.
11. Luger K, Mäder AW, Richmond RK, Sargent DF, Richmond TJ (1997) Crystal structure of the nucleosome core particle at 2.8 A resolution. *Nature* 389(6648):251–260.
12. Lee PC, Meisel D (1982) Adsorption and surface-enhanced Raman of dyes on silver and gold sols. *J Phys Chem* 86(17):3391–3395.
13. Kumar GVP, Narayana C (2007) Adapting a fluorescence microscope to perform surface enhanced Raman spectroscopy. *Curr Sci* 93:778–781.
14. Nowakowski J, et al. (2002) Structures of the cancer-related Aurora-A, FAK, and EphA2 protein kinases from nanovolume crystallography. *Structure* 10(12):1659–1667.
15. MacKerell AD, et al. (1998) All-atom empirical potential for molecular modeling and dynamics studies of proteins. *J Phys Chem B* 102(18):3586–3616.
16. Mackerell AD, Jr., Feig M, Brooks CL, 3rd (2004) Extending the treatment of backbone energetics in protein force fields: Limitations of gas-phase quantum mechanics in reproducing protein conformational distributions in molecular dynamics simulations. *J Comput Chem* 25(11):1400–1415.
17. Jorgensen WL, Chandrasekhar J, Madura JD, Impey RW, Klein ML (1983) Comparison of simple potential functions for simulating liquid water. *J Chem Phys* 79(2):926–935.
18. Darden T, York D, Pedersen L (1993) Particle mesh Ewald: An N·log(N) method for Ewald sums in large systems. *J Chem Phys* 98(12):10089–10092.
19. Ryckaert J-P, Ciccotti G, Berendsen HJC (1977) Numerical integration of the cartesian equations of motion of a system with constraints: Molecular dynamics of n-alkanes. *J Comput Phys* 23(3):327–341.
20. Morris GM, et al. (2009) AutoDock4 and AutoDockTools4: Automated docking with selective receptor flexibility. *J Comput Chem* 30(16):2785–2791.
21. Sanner MF (1999) Python: A programming language for software integration and development. *J Mol Graph Model* 17(1):57–61.
22. Morris GM, et al. (1998) Automated docking using a Lamarckian genetic algorithm and an empirical binding free energy function. *J Comput Chem* 19(14):1639–1662.
23. Phillips JC, et al. (2005) Scalable molecular dynamics with NAMD. *J Comput Chem* 26(16):1781–1802.
24. Humphrey W, Dalke A, Schulten K (1996) VMD: Visual molecular dynamics. *J Mol Graph* 14(1):33–38, 27–28.
25. Frisch MJ, et al. (2009) *Gaussian 09, revision B.01* (Gaussian, Inc., Wallingford, CT).

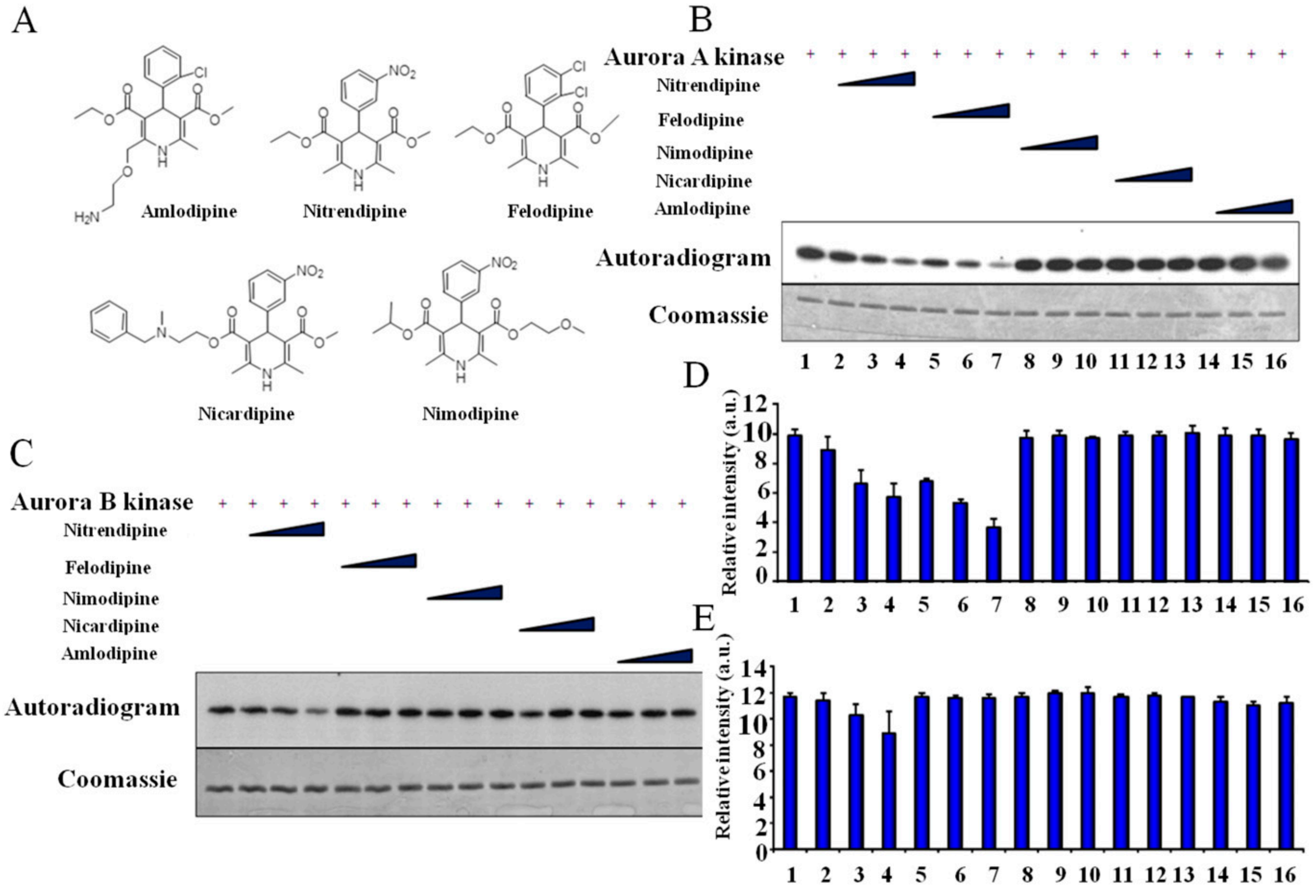

Fig. S1. Effect of dihydropyridines on Aurora kinases. A few therapeutically important dihydropyridine ring-containing compounds: (*A*) felodipine, nitrendipine, nimodipine, nicardipine, and amlodipine (F9677, N149, N7510, and A5605, respectively; purchased from Sigma) were screened against the Aurora A (*B*) and Aurora B (*C*) enzymes. Aurora A and B (40 ng) were incubated with histone H3 and 2.5 μM [γ-^{32}P] ATP in the presence of DMSO (lane 1) and an increasing (15, 30, and 60 μM) concentration of nitrendipine (lanes 2–4), felodipine (lanes 5–7), nimodipine (lanes 8–10), nicardipine (lanes 11–13), and amlodipine (lanes 14–16). I represents the autoradiogram and II shows the corresponding coomassie- stained gel. *D* and *E* represent the extent of phosphorylation in the similar sets of reactions for Aurora A and B, respectively (as previously described). Error bars represent SDs calculated for three independent experiments.

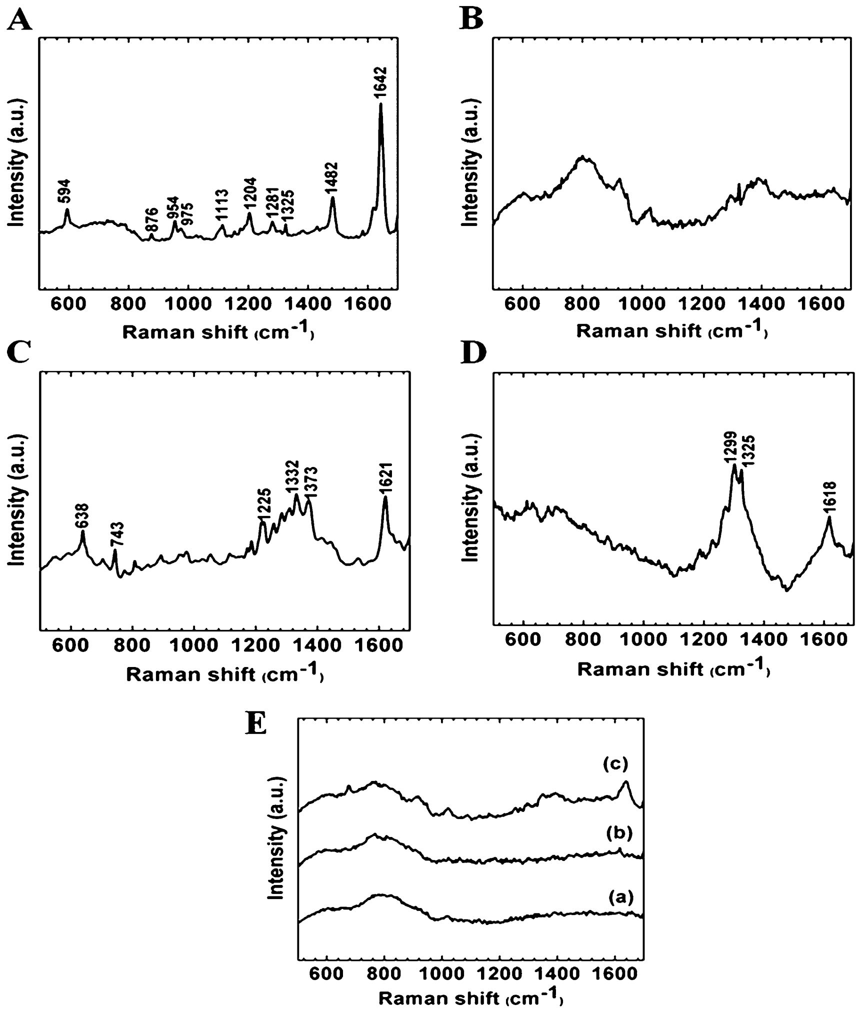

Fig. S2. (*A*) Raman spectra of felodipine and (*B*) SERS spectra of felodipine. (*C*) Raman spectra of reversine. (*D*) SERS spectra of reversine and (*E*) SERS spectra of the silver nanoparticle in aqueous solution (a), protein buffer (b), and protein buffer containing DMSO (c).

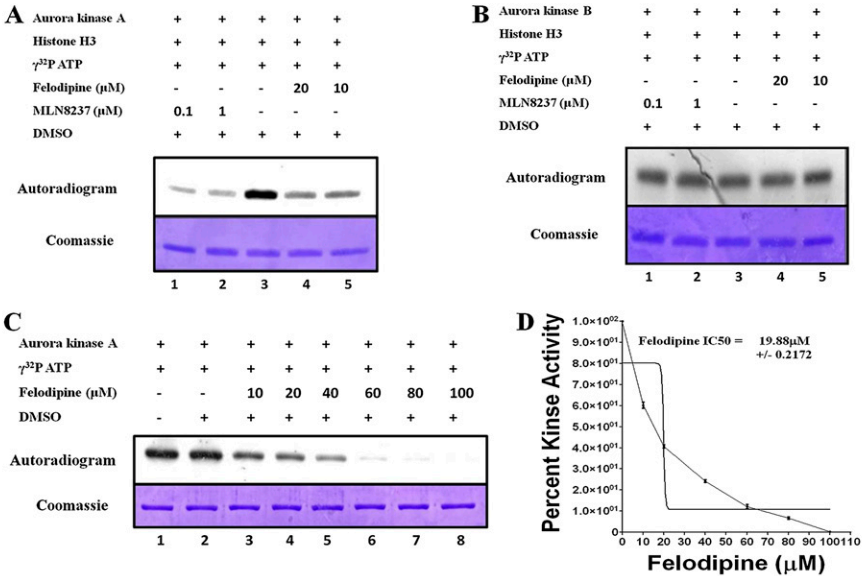

Fig. S3. (*A*) Kinase assays were performed in the presence of 10 and 20 μM of felodipine or 0.1 and 1 μM of MLN8237, a known specific inhibitor of Aurora A kinase. Histone H3 with AURA and [γ-^{32}P] ATP in the presence of DMSO (lane 3)/felodipine 10 and 20 μM (lanes 4 and 5), or MLN8237 0.1 and 1 μM (lanes 1 and 2). (*B*) Felodipine and MLN8237 could not inhibit the kinase activity of Aurora kinase B. Recombinant histone H3 with AURB, [γ-^{32}P] ATP, and in the presence of DMSO (lane 3), and felodipine 10 and 20 μM (lanes 4 and 5), or MLN8237 0.1 and 1 μM (lanes 1 and 2). (*C*) Kinase assays were performed for Aurora A (40 ng) in the presence of an increasing concentration of felodipine: the enzyme alone (lane 1), enzyme and DMSO (lane 2), and the enzyme with an increasing concentration of felodipine of 10, 20, 40, 60, 80, and 100 μM (lanes 3–8). (*D*) The quantitative representation of relative intensities of the radioactive signal was plotted using the average value of relative activity (%) against the concentration of felodipine for the technical triplicates performed. Error bars represent SDs. IC$_{50}$ was calculated using the graph as 19.88 ± 0.2172 μM.

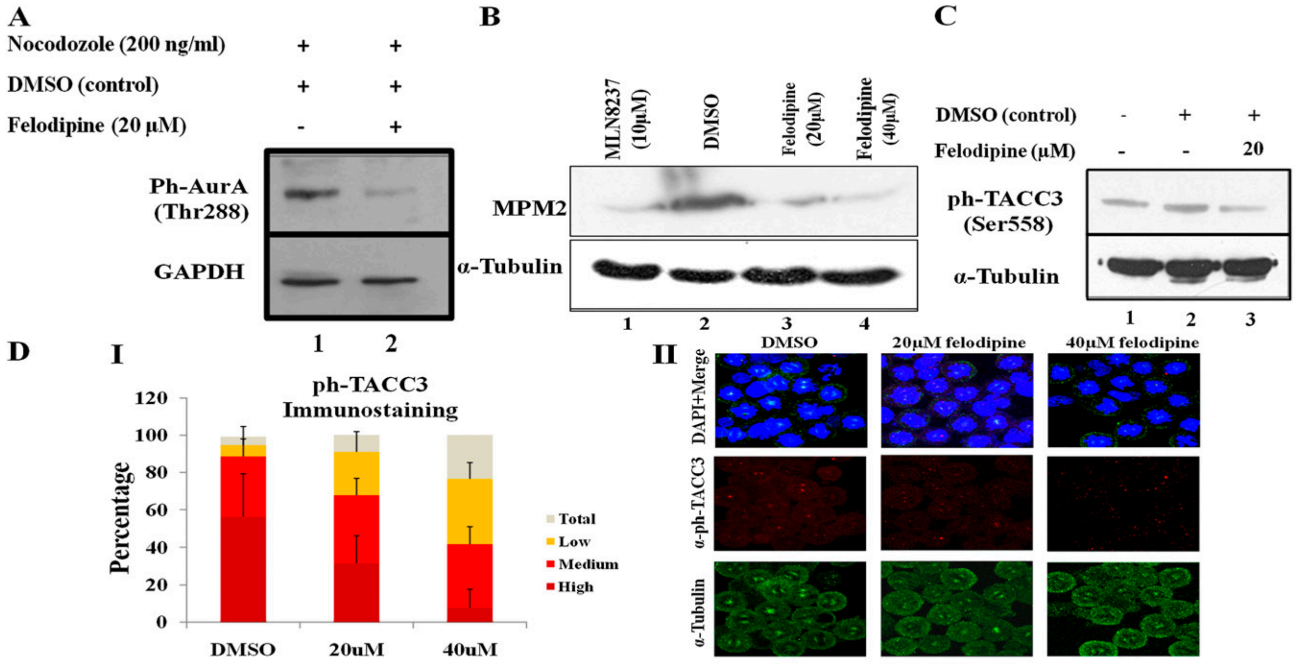

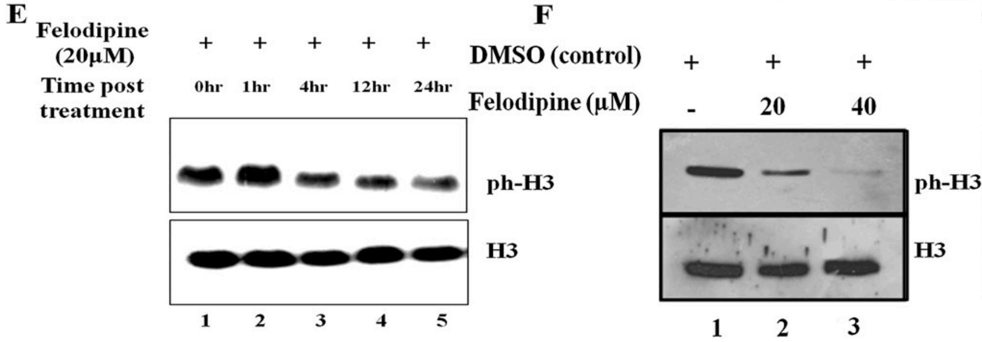

G

Cell Lines	Aurora A IC50 (μM) (Ph-AurA-T288)	Aurora B IC50 (μM) (ph-H3-S10)
HeLa S3	6.19±0.20	12.42±0.13
HEK293T	6.12±0.17	12.86±0.14
MCF7	6.05±0.22	12.92±0.25
HCT116	6.16±0.20	25.07±0.16
C6	6.08±0.20	12.31±0.10

Fig. S4. (*A*) Lysates from HeLa cells preexposed to nocodazole and treated with the indicated concentration of felodipine and DMSO with 20 μM MG132 for 3 h in the presence of nocodazole were subjected to the Western blot analysis using the indicated antibody and GAPDH as the loading control. (*B*) Western blot analysis of HeLa cells lysates prepared after 24 h of treatment with the indicated compounds using MPM2 antibody and α-tubulin (loading control). (*C*) Felodipine shows inhibition of TACC3 phosphorylation. Western blot analysis was performed with untreated, DMSO, and felodipine-treated whole-cell extracts using phospho-TACC3 antibody and α-tubulin antibody (loading control). (*D*) In a parallel assay, immunofluorescence staining of the cells treated with the indicated compounds was performed using ph-TACC3 antibody and α-tubulin to capture the dividing cells. Based on the staining intensity of the images, scoring was done with a low cutoff intensity of 0–50, a medium cutoff intensity of 50–150, and a high cutoff intensity of 150 to 200, and tabulated as bar chart in *D*, *I*. Error bars represent SDs. The representative images, under 63× magnification, are shown in *D*, *II*. *E* shows the Western blot analysis of cell lysates prepared from cells posttreatment with the indicated time using ph-H3 and H3 (loading control) antibodies. (*F*) Similarly, lysates from HeLa cells treated with either DMSO only (lane 1) or the indicated concentration of felodipine for 24 h were subjected to the Western blot analysis using ph-H3 antibody and H3 antibody (loading control). (*G*) Intracellular IC_{50} traced by the indicated antibodies for Aurora A and B kinases by immunofluorescence and Western blot analysis, respectively, are tabulated.

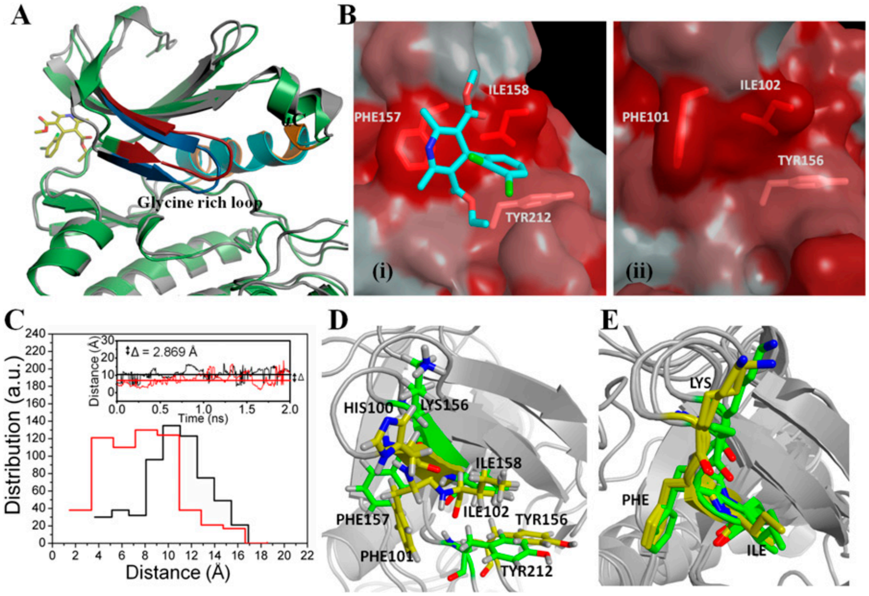

Fig. S5. (*A*) Superimposed structures of Aurora A after 2 ns of MD simulation with (gray) and without (green) felodipine. The glycine-rich loop region undergoes change in conformation (colored in red and blue to denote free and felodipine-bound, respectively). The αC region is colored in orange (free) and cyan (felodipine-bound). (*B*) Binding region of felodipine to Aurora A (*i*) and the corresponding site in Aurora B (*ii*) represented by Eisenberg's hydrophobicity index. The felodipine bound to Aurora A is shown in stick representation. (*C*) rmsd distances between center of masses of residues Phe-157 and Ile-158 (Aurora A is black) and Phe-101 and Ile-102 (Aurora B is red) obtained in 400 frames of a 2-ns MD simulation plotted as a histogram. *Inset* shows the variation in the rmsd distance between center of masses of Phe-157 and Ile-158 (Aurora A, in black) and Phe-101 and Ile-102 (Aurora B, in red) as a function of time. The mean averages of these distances are shown as solid lines. The difference in mean average was 2.869 Å. (*D*) Superimposed felodipine-binding pocket of 1-ns equilibrated structures of human Aurora A and the corresponding pocket in human Aurora B. Key residues are shown in sticks. (*E*) Superimposed crystal structures of human Aurora A (PDB ID codes 1MQ4 and 2WTV) and *Xenopus* Aurora B (PDB ID codes 2VGO and 2BFX). The carbon atoms in Aurora A and B are colored in green and yellow, respectively. Nitrogen, oxygen, and hydrogen atoms are colored in blue, red and white, respectively in *D* and *E*.

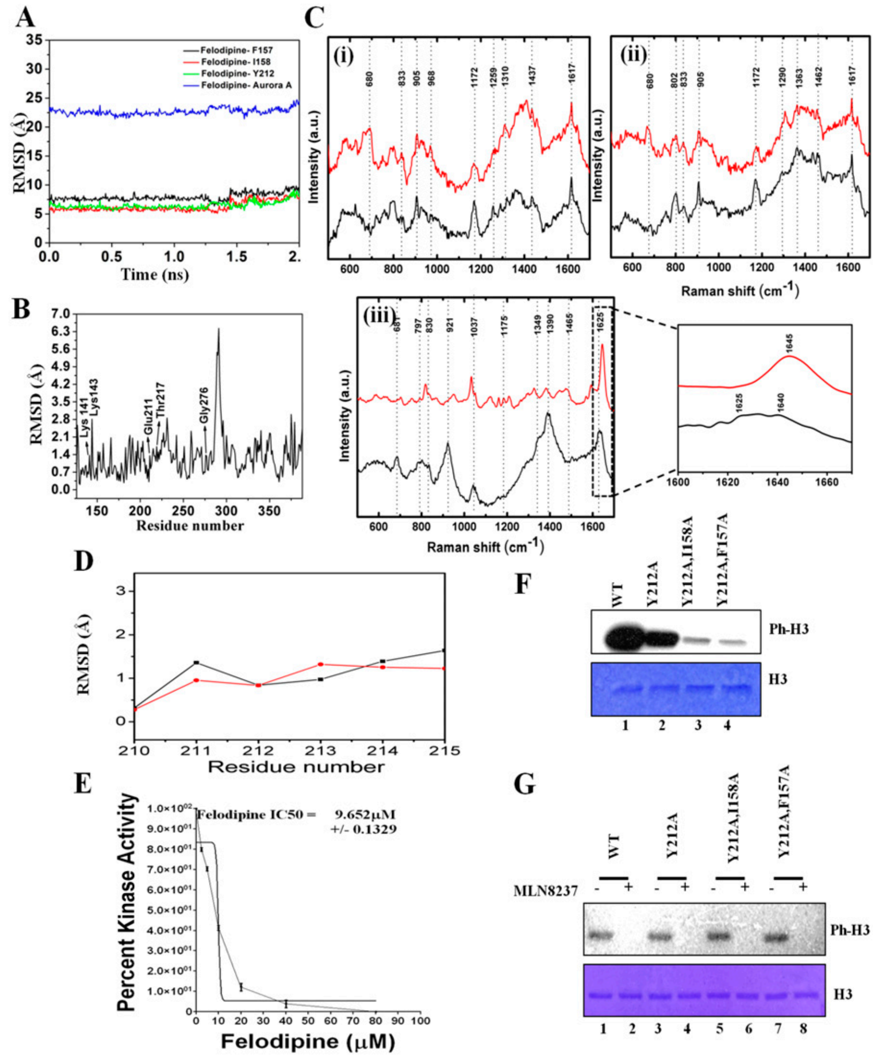

Fig. S6. (*A*) rmsd distances between felodipine and residues Phe-157 (black), Ile-158 (red), and Tyr-212 (green) and Aurora A (blue). (*B*) rmsd distances between residues after 2-ns simulation between Aurora A and Aurora A complexed with felodipine. Key residues related to the active site of Aurora A are denoted by arrows. (*C*, *i*) SERS spectra of the combinatorial mutant of Aurora A (Ile-158 and Tyr-212) in black and its complex with felodipine in red. The same data are represented for the Phe-157 and Tyr-212 mutant (*C*, *ii*) and His-201 mutant (*C*, *iii*) proteins. *C*, *Inset* highlights the amide I region of *iii* showing the shift in the amide I band from 1,625 to 1,645 cm^{-1}. (*D*) rmsd distances between the residues in the active site region (residues 210–215) of Aurora A when felodipine binds to the first site (black) and to the second site (red). (*E*) IC$_{50}$ of *E. coli*-expressed Aurora A kinase (9.652 ± 0.1329 μM) was calculated using the graph plotted using the relative intensities of the radioactive signal using the average value of relative activity (%) against the indicated concentration of felodipine for the technical triplicates performed. Error bars represent SDs. *F* represents the comparative activity of wild type versus the indicated mutant Aurora A kinases expressed in *E. coli* using the in vitro kinase assay. *G* shows the in vitro inhibition profile of the same data in the presence and absence of 0.1 μM MLN8237.

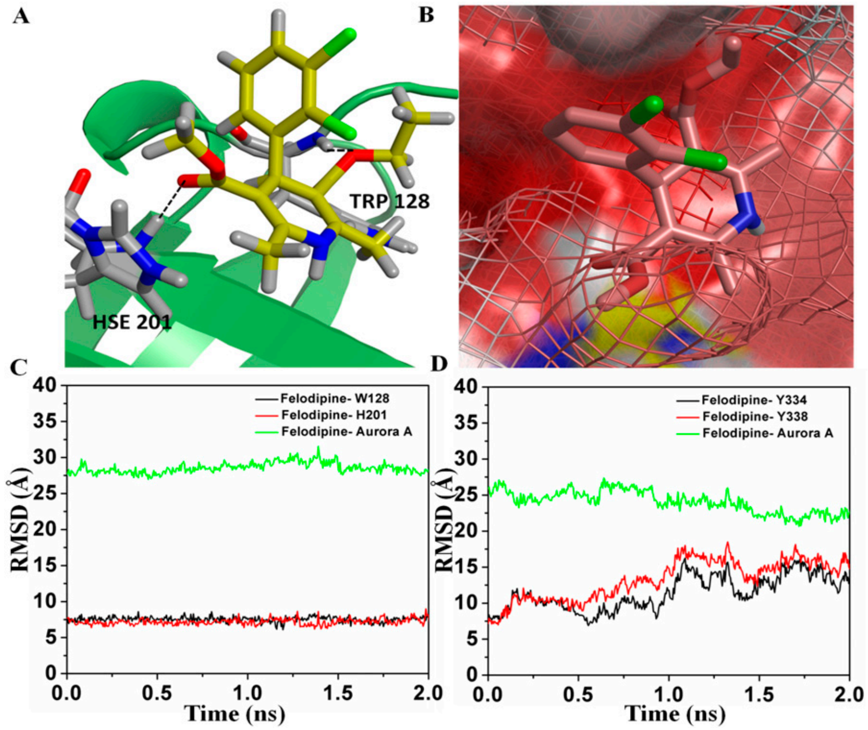

Fig. S7. (*A*) The bound configuration of felodipine to Aurora A to the second binding site. The residues colored in gray are in hydrophobic interaction with felodipine. Felodipine is hydrogen-bonded to Aurora A through residues Trp-128 and His-201 with hydrogen bond distances of 2.1 and 1.9 Å, respectively (represented by dashed line). The carbon, oxygen, nitrogen, and chlorine atoms are colored in yellow, red, blue, and green, respectively. (*B*) The surface-binding mode of felodipine to the second binding site. The Aurora B surface is shown in wireframe to highlight the difference in the hydrophobic binding site. (*C*) rmsd distances between felodipine and residues Trp-128 (black) and His-201 (red) and Aurora A (green) for the second binding site. (*D*) rmsd distances between felodipine and residues Tyr-334 (black) and Tyr-338 (red) and Aurora A (green) for the third site.

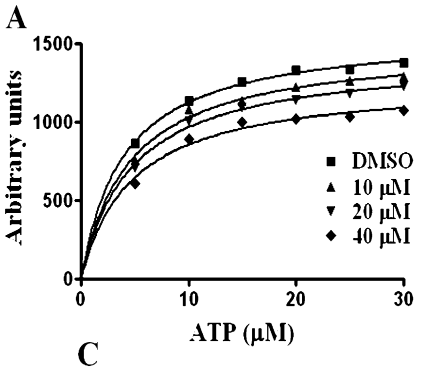

B

Felodipine (µM)	DMSO	10	20	40
Vmax	1574	1493	1419	1261
Km	3.967	4.492	4.651	4.699

C

K_a (µM)	N (Ligand/Protein)	ΔH (kcal mol^{-1})	ΔS (cal mol^{-1} K^{-1})	ΔG (kcal mol^{-1})
1.14±0.06	1.75±0.3	-3.2±0.5	18.3±1	-8.65±0.5

Fig. S8. *A* represents the Michaelis–Menten plot for the indicated concentration of felodipine against increasing amounts of ATP by maintaining a constant concentration of substrate H3 and enzyme Aurora A. The kinetic parameters obtained from the same result are tabulated in *B*. *C* represents the thermodynamic parameters for the association of felodipine with Aurora A obtained from ITC at 25° C. SDs were calculated from three independent sets of experiments.

A

Cell line	DMSO (%)	10μM Felodipine (%)	30μM Felodipine (%)
HeLa			
2N	67.41	2.14	3.32
2-4N	9.24	59.86	6.09
4N	20.88	17.59	44.88
>4N	0.77	20.79	45.93
HEK293T			
2N	55	40.79	3.71
2-4N	20.47	32.54	55.44
4N	22.52	11.27	19.79
>4N	2.25	16.87	21.54
MCF7			
2N	48.85	20.29	1.68
2-4N	32.12	50.82	59.79
4N	11.99	13.61	12.06
>4N	2.58	14.37	24.39
HCT116			
2N	41.16	43.15	4.08
2-4N	28.77	28.48	42.05
4N	24.92	22.55	12.61
>4N	4.83	3.75	32.95
C6			
2N	72.01	0.06	3.19
2-4N	12.09	5.56	0.1
4N	15.43	77.02	2.82
>4N	0.17	16.02	0.43

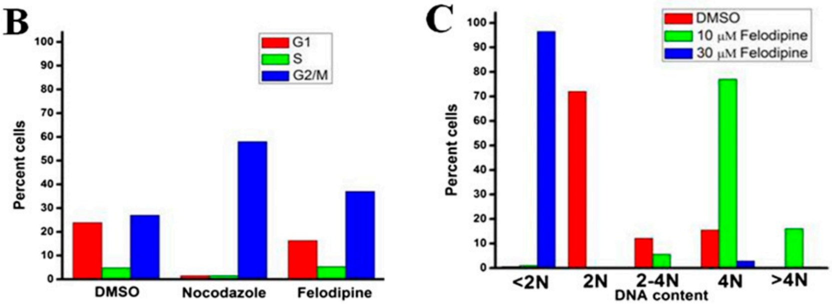

Fig. S9. Felodipine induces aneuploidy in mammalian cell lines. (*A*) Four different cell lines were treated with 10 and 30 μM felodipine and DMSO as the solvent control. The control and compound treated cells were subjected to FACS analysis using Propidium Iodide stain. The number of cells (%) with different ploidy levels (2, 2–4, 4, and >4 N) among the analyzed population in each cell line was tabulated. (*B*) HEK293T cells were treated with 100 ng/mL nocodazole to the media for 12 h and then G2/M arrested cells were collected and released in the presence of either DMSO/felodipine (20 μM)/nocodazole (100 ng/mL) and allowed to grow. After 24 h, the cells were collected and analyzed in a BD FACSCalibur for the DNA content. The number of cells (%) in each cell cycle stage among the analyzed population was plotted as a bar graph. (*C*) Similarly, the FACS analysis was performed with DMSO/felodipine-treatred C6 cells, which were plotted for the percent cells with the indicated DNA content.

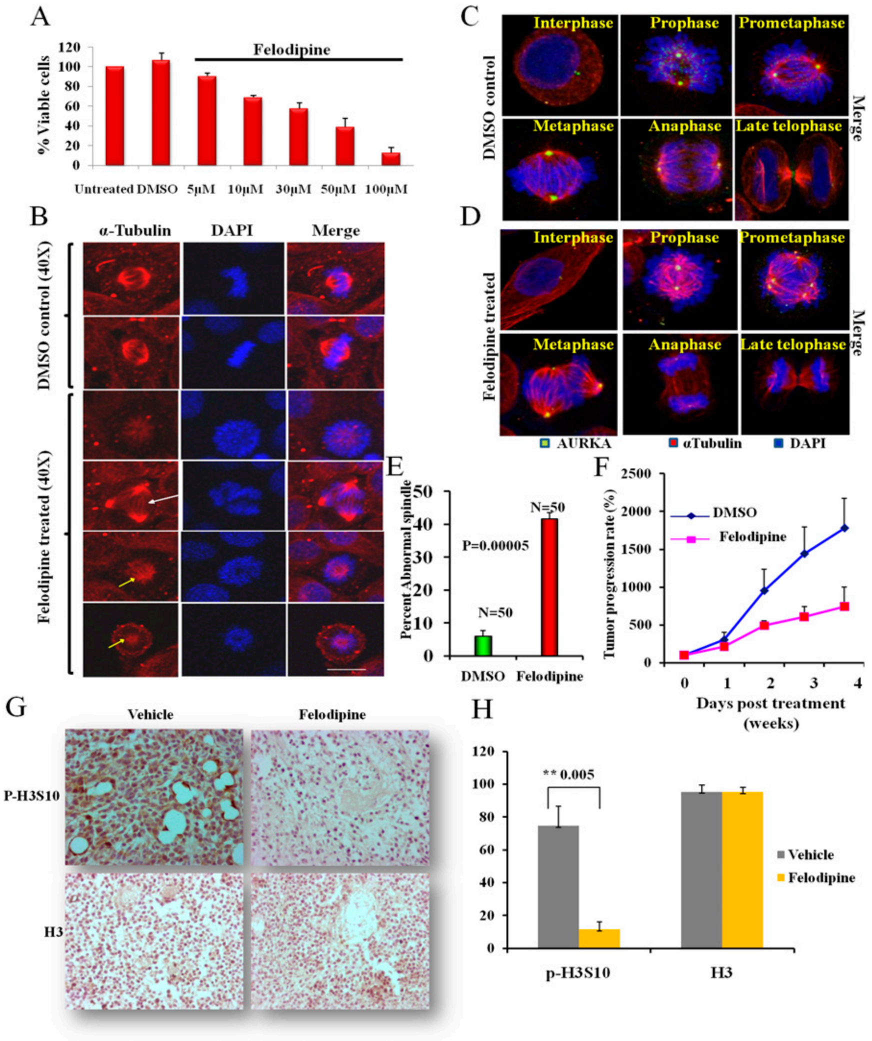

Fig. S10. Felodipine induces defects in proliferation. (*A*) HeLa cells treated with DMSO or increasing concentrations of felodipine were subjected to a cell viability assay 24 h posttreatment using MTS inert salt. The percent viable cells are plotted as bar graphs comparing untreated cells versus DMSO/felodipine-treated cells. The experiment was repeated three times and error bars plotted to obtain SDs. (*B*–*D*) HeLa cells were treated with DMSO or 10 µM felodipine for 24 h and subjected to immunofluorescence imaging using anti–α-tubulin antibodies. The DNA was visualized by Hoechst staining. Representative images at 40× magnification are depicted in *B*. (*B*). Monopolar (yellow arrows) and multipolar spindles (white arrows) are indicated. (*C* and *D*) Coimmunofluorescence images (100× magnification) showing (*C*) Aurora A (green) merged with α-tubulin (red) of DMSO versus (*D*) felodipine-treated cells captured 24 h posttreatment. (*E*) To test the statistical significance of mitotic spindle abnormalities after compound treatment, four biological replicate experiments were performed with either DMSO or 10 µM felodipine-treated HeLa cells. Metaphases ($n = 50$) were counted in each experiment. The numbers of metaphases that showed spindle defects were expressed as a ratio of the total number of metaphases counted and plotted as a bar graph for DMSO versus felodipine-treated cells. Error bars represent SDs. The *P* value calculated using the *t* test is 0.00005. (*F*) The tumor progression rate in nude mice xenografted with C6 glioma cells in the s.c. tissue of their flank region is plotted as the percent growth rate in weekly intervals posttreatment with either the vehicle control DMSO or 5 mg felodipine per kilogram of body weight daily. (*G*) IHC analysis (magnification: 40×) of the xenograft tissue from the vehicle (DMSO) versus felodipine-treated (5 mg/kg of body weight) mice at the end of the experimental period, using the indicated antibodies. The same data are represented as the percent nuclear positivity of each group in *H*.

Table S1. The relative activity of a selective panel of mitotic kinase

No.	Kinase name	Experiment 1	Experiment 2	Mean
1	ABL1 WT	89	86	87
2	AKT3	107	96	101
3	Aurora A	48	38	**43**
4	Aurora B	104	110	107
5	Aurora C	81	81	81
6	CDK4/CycD1	104	101	103
7	CHK2	99	95	97
8	EGF-R WT	55	49	52
9	ERK1	102	97	100
10	FAK aa2-1052	68	86	77
11	FGF-R1 WT	93	73	83
12	FLT3 WT	68	75	72
13	GSK3-beta	95	103	99
14	IKK-beta	101	106	104
15	LCK	45	39	**42**
16	MEK1 WT	116	138	127
17	mTOR	78	80	79
18	NEK2	117	116	116
19	p38-alpha	122	122	122
20	PAK6	121	109	115
21	PLK1	115	109	112
22	RAF1 Y340D/Y341D (untagged)	91	81	86
23	ROCK1	119	113	116
24	RPS6KA1	99	103	101
25	SRC (GST-HIS-tag)	53	52	53
26	STK33	77	77	77
27	TGFB-R2	77	86	82
28	TSF1	106	96	101
29	VEGF-R2	46	37	**41**
30	VRK2	102	108	105

Mean of the two independent experiments are shown in the last column and the relative activity (in comparison with the solvent control, DMSO) less than 50% is highlighted in boldface. Assay concentrations = 20 μM.